ORIGINAL PAPER

Computational studies on Mg ion conductivity in $Mg_{2x}Hf_{1-x}Nb(PO_4)_3$ using neural network potential

Keisuke Makino[1] · Naoto Tanibata[1] · Hayami Takeda[1] · Masanobu Nakayama[1]

Abstract

Low Mg diffusivity in solid-state oxides is an obstacle for the development of materials for Mg ion batteries, which are expected to have high capacity. In this study, we focused on NASICON-type and β-iron sulfate-type $Mg_{2x}Hf_{1-x}Nb(PO_4)_3$ that exhibit relatively high Mg ionic conductivity and investigated the Hf/Nb configuration and composition dependence of phase stability and ion conductivity by atomistic simulation using neural network potentials. The calculations show that the NASICON-type structure is slightly more stable and has higher Mg ionic conductivity than that of the β-iron sulfate-type. The effect of the Hf/Nb configuration was investigated and showed that the ordered stable structure had much lower ionic conductivity than the disordered structure. Furthermore, as the Mg ion concentration increased, the ionic conductivity increased monotonically at low concentrations but tended to converge to a constant value above a certain concentration. The saturation of the ionic conductivity despite increasing the Mg concentration may be due to the trapping effect of the Mg ions caused by the Hf vacancies as well as the Hf/Nb arrangement.

Introduction

Lithium-ion batteries are widely used nowadays in portable electronic devices and electric vehicles, owing to their high energy density and long cycle life [1]. However, the increasing mining costs associated with the rapidly growing demand for lithium resources [2] and the further improvement of energy density [3] need to be solved due to the rapid proliferation of electric vehicles. The development of Mg ion batteries is expected to solve this problem [4–7], as Mg ions are divalent and can carry two electrons in a single carrier ion, theoretically doubling the energy density [8, 9]. This has the potential to realize EVs with a cruising range that surpasses that of conventional vehicles. Furthermore, safety can also be ensured if an all-solid-state magnesium ion battery is realized in which the flammable organic electrolyte is replaced by a solid electrolyte [8–10].

However, the higher the valence of the conductive ion species, the stronger the Coulomb interaction with the surrounding counter ions and the lower the conductivity of the ion [11]. Therefore, research has focused on monovalent cation conductors such as Li^+ and Na^+ and high-performance electrochemical devices have been successfully developed [12–16]. Therefore, in order to develop future Mg ion all-solid-state batteries, the electrode and solid electrolyte structures must be optimized to overcome the poor conductivity of Mg ions because of the divalent Mg ions.

It is known from the literature [17–21] that phosphate materials are promising ionic conductors for Mg ions. For example, Imanaka et al. reported that $Mg_{0.7}(Zr_{0.85}Nb_{0.15})_4(PO_4)_6$ with a β-iron sulfate structure showed a relatively high Mg ion conductivity of 1.1×10^{-7} S cm^{-1} at 573 K [22]. We have reported that the polymorphic NASICON-type $Mg_{0.5}Zr_2(PO_4)_3$ has an even higher ionic conductivity than the β-iron sulfate-type $Mg_{0.5}Zr_2(PO_4)_3$ by performing a first-principles molecular dynamics study, although the NASICON-type polymorph is thermodynamically unstable [23]. Recently, an Mg ionic conductor with a NASICON-type $HfNb(PO_4)_3$ compositional framework was reported to have a higher ionic conductivity of 2.1×10^{-6} S cm^{-1} at 573 K than the β-iron sulfate-type $Mg_{0.7}(Zr_{0.85}Nb_{0.15})_4(PO_4)_6$ [24].

✉ Masanobu Nakayama
masanobu@nitech.ac.jp

[1] Department of Advanced Ceramics, Nagoya Institute of Technology, Nagoya, Aichi 466-8555, Japan

The NASICON-type structure in $HfNb(PO_4)_3$ consists of $(Nb, Hf)O_6$ octahedra and PO_4 tetrahedra alternately bridged by O atoms at the two coordination ends, forming $(Hf, Nb)_2P_3O_{18}$ (lantern) units (Fig. 1). The Mg ions migrate between lattice sites in the corner sharing network. For this local bonding rule, another type of structure with a different network topology, known as a β-iron sulfate-type structure, is also derived [25, 26].

The superior Mg ion conductivity in the NASICON-type structure is attributed to the ordered arrangement of the lantern units in the NASICON phase, whereas the lantern units in the β-iron sulfate phase are slightly distorted [27]. However, in the case of $Mg_{0.5}Zr_2(PO_4)_3$ presented above, it has been reported that the NASICON phase is stable only under negative pressure conditions and the β-iron sulfate phase is stable in real systems [23]. However, as mentioned above, it is interesting that successful synthesis of the NASICON phase has been achieved in $HfNb(PO_4)_3$ doped with MgO, resulting in $(Mg_{0.1}Hf_{0.9})_{4/3.8}Nb(PO_4)_3$ [24].

In this study, we focus on the $HfNb(PO_4)_3$ phase with the NASICON phase and investigate the phase stability, quantitative evaluation of ionic conductivity, and details of the conduction mechanism using molecular dynamics (MD) simulations with the neural network potential (NNP) force field (FF).

Currently, first-principles molecular dynamics (FPMD) simulations are one of the approved methods for evaluating the diffusivity of focused ions in solid-state, but are limited to the application of a few hundred atoms and simulation times of a few tens of picoseconds due to the high computational cost. Therefore, the statistics for ion hopping events may not be sufficient to simulate the ionic conductivities of less diffusive atoms such as divalent ions including hMg^{2+}. However, in recent years, NNP methods have enabled calculations of large size and long simulation time with an accuracy comparable to density functional theory (DFT) [28].

This should allow a more accurate and efficient investigation of Mg diffusivity.

Methods

The $Mg_{2x}Hf_{1-x}Nb(PO_4)_3$ composition, in which Hf and Nb occupy the octahedral site and P occupies the tetrahedral site, was the subject of this study. The initial structure used for the calculations was based on our previous report on $Mg_{0.5}Zr_2(PO_4)_3$ [23]. All octahedral Zr ions in the structure of $Mg_{0.5}Zr_2(PO_4)_3$ with NASICON-type and β-iron sulfate-type structures were replaced by Hf and Nb ions, respectively, in a 1:1 molar ratio. In addition, Hf vacancies were introduced to keep charge neutrality with the introduction of Mg ions at the center of the lantern site (6a site in Fig. 1) to construct NASICON-type and β-iron sulfate-type structures with the $Mg_{2x}Hf_{1-x}Nb(PO_4)_3$ composition. We prepared superstructures for the molecular dynamics (MD) simulation such that the number of atoms is about 1500 in the NASICON phase and about 1100 in the β-iron sulfate phase. In this paper, the NASICON phase is referred to as the α-phase and the β-iron sulfate phase as the β-phase, hereafter.

NNP is used to calculate the energy and forces acting on ions for a given structure. A pretrained universal interatomic potential implemented in M3GNet.py software is used [29]. The structure relaxation and the MD simulations under the canonical ensemble (NVT) are performed using the atomic simulation environment (ASE) [30]. NVT-MD simulations were performed for 100 picoseconds with a time step of 1 fs, after the structure relaxation, unless specifically mentioned. Note that the validity of the NNP is confirmed by comparison with energies or forces obtained by density functional theory (DFT) calculations. The DFT calculations were performed using the plane-wave basis and projector-augmented wave methods [31], which are implemented in the Vienna ab initio simulation package (VASP) [32–34]. In

Fig. 1 **a** NASICON-type structure and **b** β-iron sulfate-type structure of $HfNb(PO_4)_3$. Green and lavender polyhedra correspond to $(Hf,Nb)O_6$ and PO_4, respectively. Orange and gray spheres correspond to Mg ion sites. Lantern units are also indicated by the hatched circle

(a) NASICON-type

Lantern unit
6a
18e
PO_4
$(Hf, Nb)O_6$

(b) β-iron sulfate-type

4d
4e
8f
Lantern unit
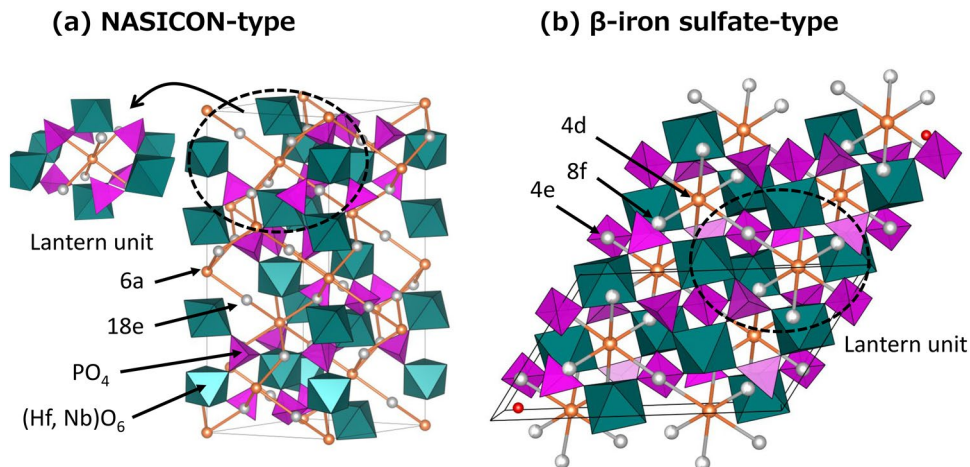
Fig. 2 Comparison of DFT and NNP calculated energies and forces for (**a**) α-phase ($x=0.17$), (**b**) α-phase ($x=0.33$), (**c**) β-phase ($x=0.19$), and (**d**) β-phase ($x=0.31$)
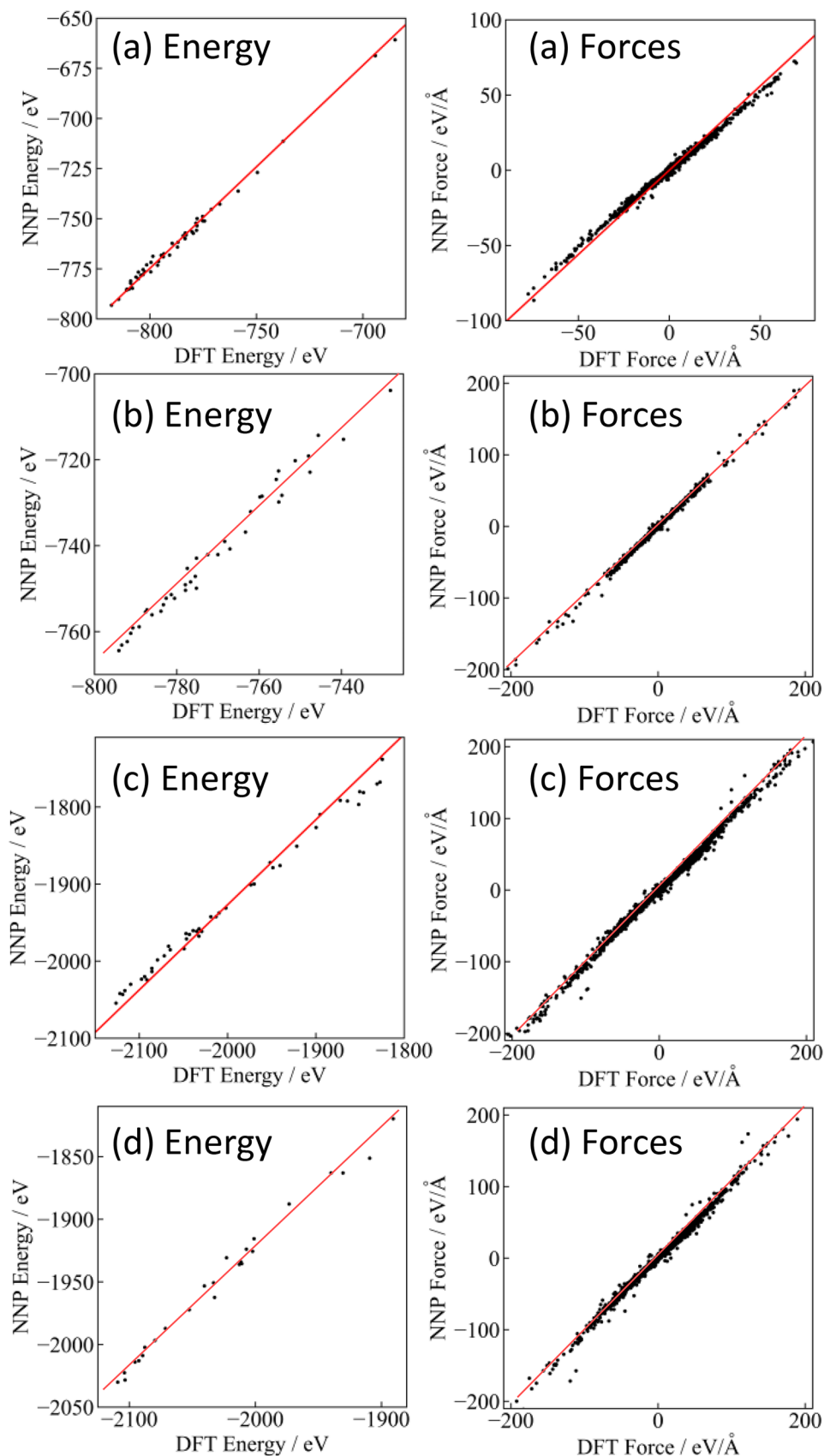
addition, the Perdew–Burke–Ernzerhof generalized gradient approximation for solids (GGA-PBEsol) [35, 36] was used to approximate the electron–electron interactions [37].

The genetic algorithm (GA) was used to optimize the Hf/Nb arrangement which was regarded as a one-dimensional string (chromosome) consisting of two labels, 0 (Hf) and 1 (Nb). The labels are randomly assigned to each cation site to the chromosome in the first generation. The structures with the most stable Hf/Nb configuration were investigated by generating offsprings using crossover and mutation operations for more energetically stable chromosome. Evaluation of the generated chromosome was performed by NNP energy calculations. The technical details of the genetic algorithm are described in our previous publications [38–40], and the in-house Python code software for genetic algorithm, GmAte.py [41] is used in the present study.

Results and discussion

The accuracy of the NNP calculation was verified by comparison with DFT calculations. Specifically, relatively small superstructures of α-phase and β-phase were created, and the lattice parameters and the positions of the consisting atoms were randomly displaced within a trace amount. A total of 50 structures were generated in this way and the calculated energies and forces acting on the atoms were compared with DFT and NNP (without structural relaxation). This operation was evaluated for $x = 0.17$ and $x = 0.33$ for the α-phase and $x = 0.19$ and $x = 0.31$ for the β-phase, respectively. Figure 2 shows the diagnostic plot, and the slope and coefficient of determination R^2 are also close to 1, confirming the potential validity of the NNP.

Stable structures with non-Mg containing $HfNb(PO_4)_3$ compositions were investigated for each of the α- and β-phases. Specifically, two types of Hf/Nb arrangements were calculated, one with an optimized Hf/Nb sequence using a GA and the other with a randomly arranged Hf/Nb sequence. The calculated energies are presented in Table 1. In both the α- and β-phases, the GA structures exhibited smaller structural energies and were more stable, although the difference was only about 7 meV/atom for the same composition. Since the material was experimentally synthesized at high temperatures (1473 ~ 1573 K), Hf/Nb is expected to form random arrays when configuration entropy effects and other factors are taken into account.

Next, the composition dependence of phase stability was evaluated for α- and β-phases with random Hf/Nb arrangement. Structural relaxation calculations were performed for each structure with varying Mg concentration (x), and the results of comparing the structural energies (eV atom^{-1}) of both phases are shown in Fig. 3. The α-phase became more stable than the β-phase as the

Table 1 Comparison of the structural energies of GA and random structures for α- and β-phases, respectively

| Sample	Structural energy per atom/eV per atom
α (GA)	−8.232
α (Random)	−8.225
β (GA)	−8.229
β (Random)	−8.222

Mg concentration x increased. However, previous reports have suggested that decomposition reactions proceed for $x > 0.05$ to form $NbPO_5$ and HfP_2O_7 in the stable α-$Mg_{2x}Hf_{1-x}Nb(PO_4)_3$ phase [24]. Therefore, increasing the amount of Mg would make it difficult to maintain the $HfNb(PO_4)_3$ matrix phase due to decomposition reactions, which are not considered in this calculation.

The dependence of the ionic conductivity on the Hf/Nb arrangement for α- and β-phases ($x = 0.05$) was investigated by comparing the NNP-MD derived ionic conductivity of Mg with GA optimized and randomly assigned Hf/Nb configurations. The total MD simulation time is 2000 ps with a time step of 1 fs. The mean square displacements (MSD) for all constituent atoms (Mg, Hf, Nb, P, and O) were calculated and the diffusion coefficients were determined from the slope of MSD plots. Figure 4 shows the MSD plots for (a) α-phase ($x = 0.05$) and (b) β-phase ($x = 0.05$). For Mg ions, the linear increase in MSD over simulation time is visible, indicating diffusion through site-to-site hopping. On the other hand, the MSD for Hf,
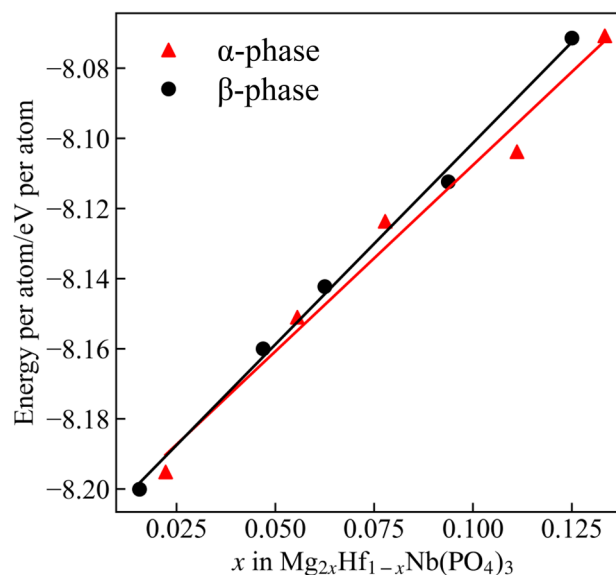
Fig. 3 Comparison of phase stability between α- and β-phases as a function of composition x

(a)

(b)
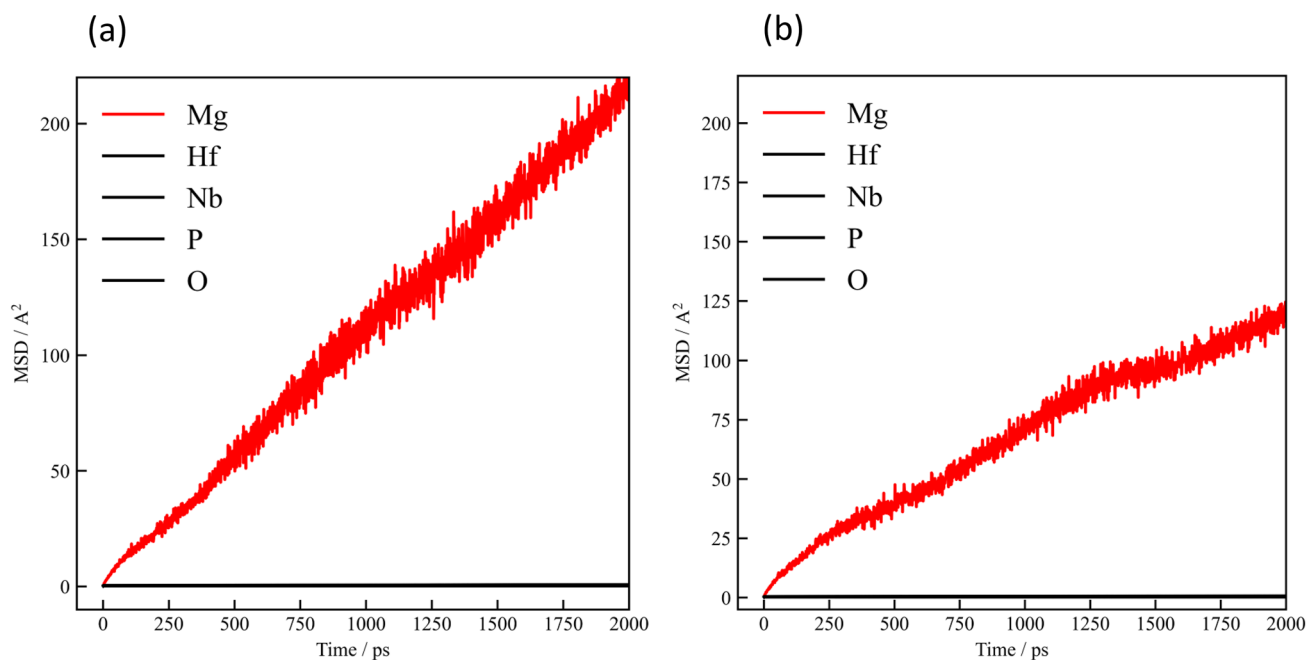
Fig. 4 MSD plots of Mg, Hf, Nb, P, and O trajectories in **a** α-phase ($x=0.05$) and **b** β-phase ($x=0.05$) at 1600 K

Nb, P, and O remained constant at around 1 Å^2, which corresponds to thermal vibrations. Note that the MSD profile for the β-phase shows the result of averaging two NNP-MD calculations performed under the same input conditions. This was necessary because obtaining a statistically linear MSD profile was challenging due to the low number of Mg ions in the lattice.

Arrhenius plots were made for these structures and the migration energies and diffusion coefficients, D, at 873 K were calculated for the diffusion of Mg. The ionic conductivity of Mg, σ, is also estimated by the Nernst-Einstein equation:

$$\sigma = \frac{z^2 F^2 c}{RT} D \qquad (1)$$

where R, T, z, F, and c are the gas constant, absolute temperature, ion valence, Faraday constant, and ion concentration, respectively.

Table 2 lists the Mg ionic conductivities and migration energies. It was confirmed that for both the random and GA structures, the α-phase at $x=0.05$ is expected to have a

higher Mg ionic conductivity than the β-phase. It was also confirmed that the structure optimized by GA has a significant decrease in Mg ionic conductivity and an increase in migration energy when compared to the random structure. This indicates that the order of the Hf/Nb arrangement is crucial for Mg ion conduction, so that experimental high-temperature sintering and quenching processes that preserve the random structure would be advantageous.

The calculated ionic conductivity of the α-phase with random structure at 873 K was in good agreement with the previously reported value of 1.2×10^{-4} S cm^{-1}. The corresponding migration energy was also in good agreement with the previously reported value of 0.68 eV [24]. This indicates the validity of our calculations and suggests that the experimental evaluation of the α-phase reported in the past suggests that the Hf/Nb arrangements are random. Note that the present computationally determined Mg ionic conductivity only accounts for Mg diffusion, whereas the experimental one includes bulk and grain boundary contributions. From the agreement between the experimental and computational conductivities, it can be inferred

Table 2 Migration energies and ionic conductivities at 873 K for GA and random structures of $Mg_{2x}Hf_{1-x}Nb(PO_4)_3$ ($x=0.05$) α- and β-phases, respectively

Sample	Migration energy, eV	Conductivity at 873 K, S cm^{-1}
α-$Mg_{2x}Hf_{1-x}Nb(PO_4)_3$ ($x=0.05$) random	0.64	9.62×10^{-5}
α-$Mg_{2x}Hf_{1-x}Nb(PO_4)_3$ ($x=0.05$) GA	0.82	6.37×10^{-6}
β-$Mg_{2x}Hf_{1-x}Nb(PO_4)_3$ ($x=0.05$) random	0.72	1.83×10^{-5}
β-$Mg_{2x}Hf_{1-x}Nb(PO_4)_3$ ($x=0.05$) GA	1.37	1.62×10^{-9}

that the grain boundary contributions are less important for the overall ionic conductivity, i.e., the coulombic interaction between the multivalent Mg^{2+} ion and the lattice is dominant for the overall conductivity performance.

In response to this result, RDF analysis was performed to investigate the interaction between Mg and the host lattice at the atomic level during Mg diffusion. The results of the RDF analysis of Mg-Nb and Mg-Hf interactions are shown in Fig. 5, and confirm the selective Mg occupation in the vicinity of Hf ions. This is due to the relative attraction of Mg ions to lower valent Hf^{4+} ions than Nb^{5+}, which reduces coulombic repulsion. This corresponds to a trapping effect on Mg ion conduction, leading to a decrease in conductivity. However, this tendency was particularly pronounced in the random structure with high ionic conductivity, as the intensity of the Mg-Hf first proximity RDF peak in the GA-derived structure is lower than in the random structure. Hence, it is difficult to explain the difference in ionic conductivity by the trapping effect, since a trapping effect often causes the reduction of ionic conductivity, in general.

Figure 6 shows the crystal structures of the random and GA-derived structures. The GA-optimized structure has an arrangement in which two adjacent HfO_6 octahedra and two

adjacent NbO_6 octahedra appear alternately in both the α- and β-phases. In addition, Fig. 7 shows the results of the RDF analysis between Nb-Nb, Hf-Hf, and Hf-Nb for both the random structure and the GA-optimized structure. In the α-phase, the first nearest Nb-Nb and Hf-Hf peaks (~5.0 Å) in the GA-optimized structure are larger than those in the random structure, while the peaks from the second nearest neighbors (~5.7 Å) disappear. This suggests that arrangements in which two NbO_6 (or HfO_6) octahedra are adjacent to each other are more likely to form. In the β-phase, the interactions between Nb-Nb and Hf-Hf around 6.3 Å are prominent in the random arrangement, whereas in the GA structure, the interactions between Nb-Hf become dominant around 6.3 Å. The difference in RDF profiles between the GA structure and the random structure appears up to around 10 Å, revealing that an ordered arrangement of Hf/Nb forms over relatively long distances.

From the RDF of Hf-Mg shown in Fig. 5, it is evident that Mg ions tend to diffuse preferentially around Hf in the random Hf/Nb array structure. For this, we conclude that the Hf ions may form a (percolation) network between both ends of the lattice, which secures the conduction pathways for the Mg ions and exhibits a higher ionic conductivity. Conversely,

Fig. 5 RDFs during Mg diffusion of Hf-Mg and Nb-Mg in **a** α-phase with Hf/Nb random, **b** β-phase with Hf/Nb random, **c** α-phase with Hf/Nb GA-optimized, and **d** β-phase with Hf/Nb GA-optimized structures
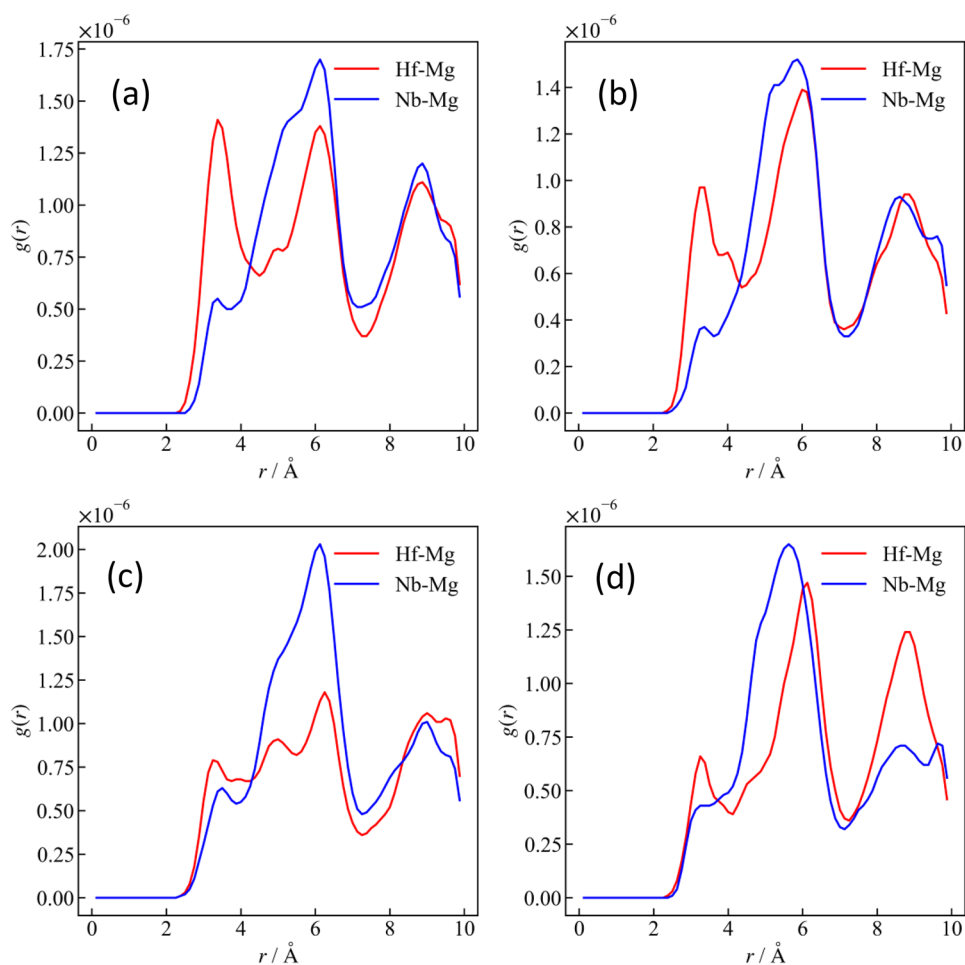
Fig. 6 NNP-optimized structures of **a** α-phase with Hf/Nb random, **b** β-phase with Hf/Nb random, **c** α-phase with Hf/Nb GA-optimized, and **d** β-phase with Hf/Nb GA-optimized structures. Beige, green, and lavender polyhedra correspond to HfO_6, NbO_6, and PO_4, respectively
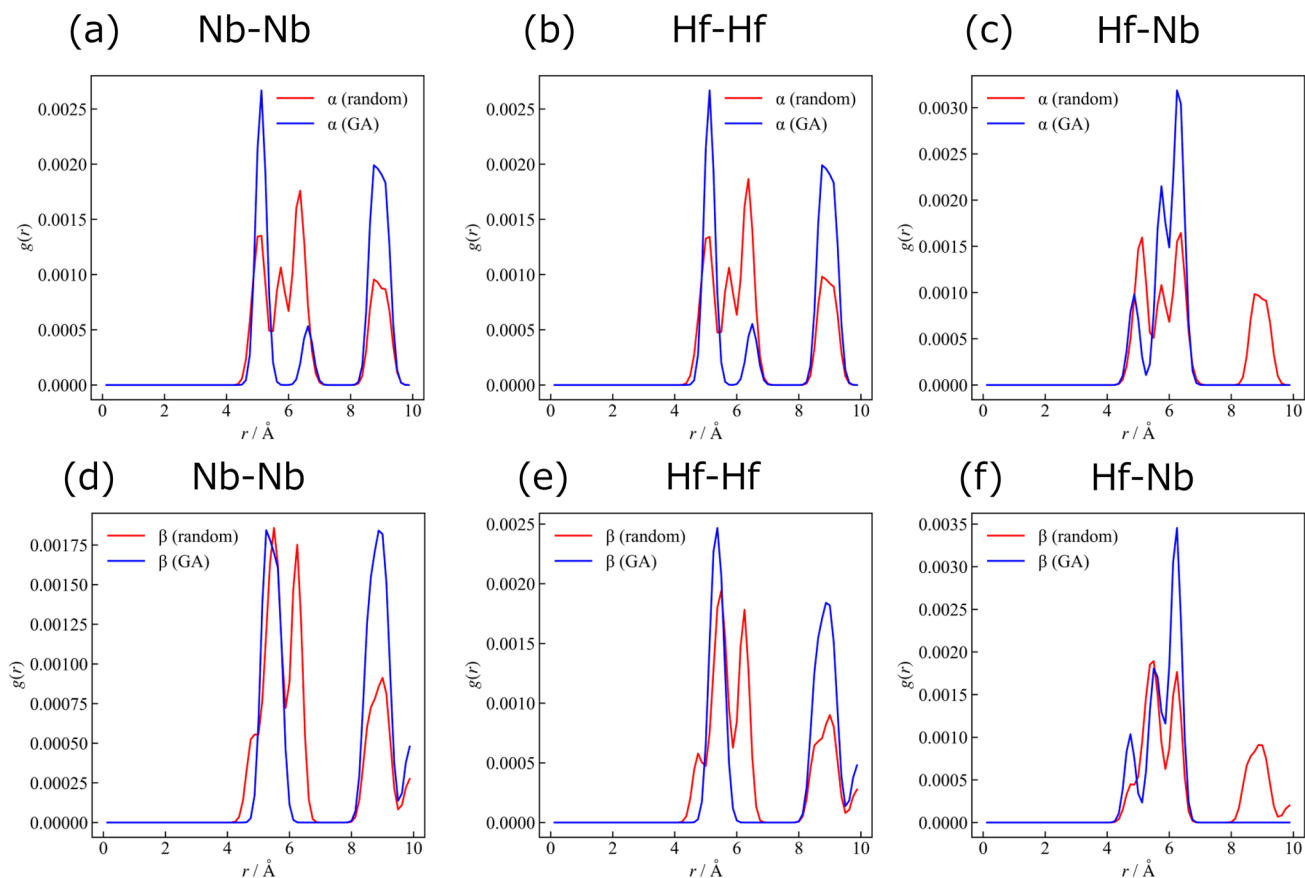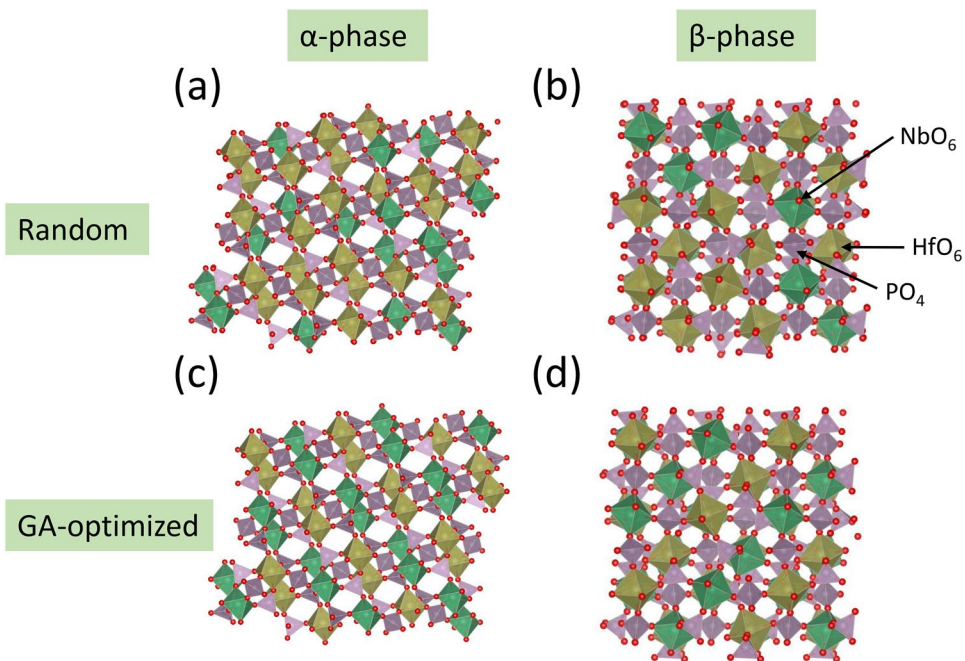
Fig. 7 RDF of **a** Nb-Nb, **b** Hf-Hf, and **c** Hf-Nb for α-phase ($x = 0.05$) with Hf/Nb random (red) and Hf/Nb GA-optimized (blue) structures. RDF of **d** Nb-Nb, **e** Hf-Hf, and **f** Hf-Nb for β-phase ($x = 0.05$) with Hf/Nb random (red) and Hf/Nb GA-optimized (blue) structures

Fig. 8 Arrhenius plots of the NNP-MD derived Mg ion conductivity for **a** α-phase and **b** β-phase with different composition x
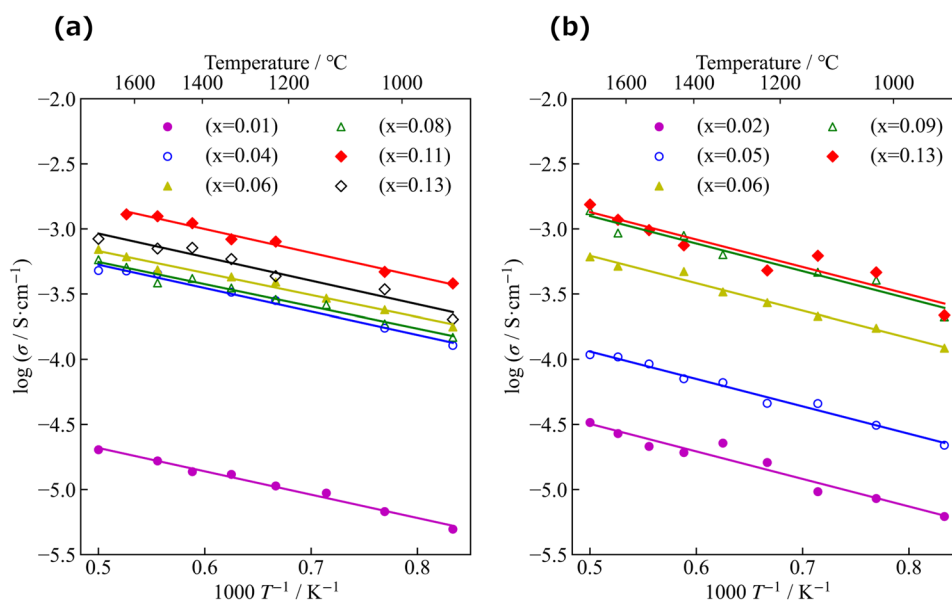
in the GA-derived Hf/Nb sequence, the Hf network is disrupted, and the conduction of Mg ions is considered to be suppressed. According to the RDF of Hf-Hf in Fig. 7, the interaction at 5.7 Å in the α-phase and the interaction at 6.3 Å in the β-phase are lost in the GA-derived structure. This suggests that the HfO_6 network is disrupted, which could hinder the conduction of Mg ions.

Next, NNP-MD simulations were performed at intervals of 100 K between 1200 and 2000 K for each composition x of α- and β-$Mg_{2x}Hf_{1-x}Nb(PO)_3$ with the Hf/Nb random structure, and the logarithm of the calculated ionic conductivity was taken. These values were plotted against the reciprocal temperature, i.e., an Arrhenius plot (Fig. 8).

In this study, we evaluated the hopping of the divalent cation Mg, which has a high migration energy, and also the number of Mg is extremely limited. Therefore, the probability of hopping events at room temperature is extremely low, and the evaluation was conducted by increasing the

simulation temperature in order to increase the number of hopping events sufficiently. In addition, from this Arrhenius plot, the activation energy and the ionic conductivity at 873 K were extrapolated, which correspond to the composition x, and are shown in Fig. 9 and Table 3.

As listed in Tables 3 and 4, the migration energy is almost constant for all compositions, about 0.66 eV for the α-phase and 0.72 eV for the β-phase. Because of the small concentration of Mg ions in the present model, the interaction between Mg ions would be small, so that the hopping of Mg can be attributed only to the interaction with the host structure $HfNb(PO_4)_3$. Hence, the change in migration energy with respect to Mg content is considered to be small.

Figure 9 and Tables 3 and 4 show the Mg ionic conductivity at 873 K as a function of Mg content, and higher ionic conductivities are confirmed for the α-phase than for the β-phase. This may be attributed to the higher migration energy of the β-phase and the stronger interaction between

Fig. 9 Compositional dependence of the Mg ion conductivity in **a** α-phase and **b** β-phase at 873 K
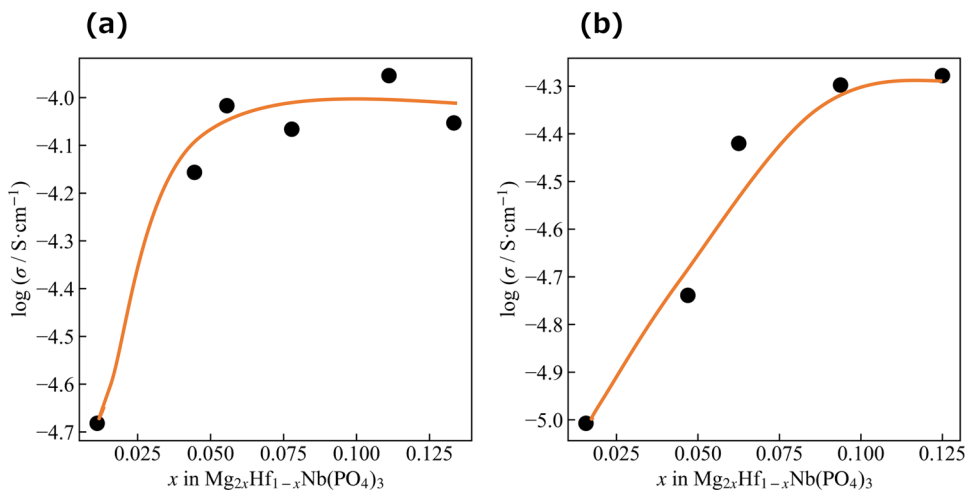
Table 3 Compositional dependence of migration energies and ionic conductivities of Mg ions for random structures of α-phases at 873 K

x in α-phase	Migration energy, eV	Conductivity at 873 K, S cm^{-1}
0.01	0.66	1.74×10^{-5}
0.04	0.66	6.98×10^{-5}
0.06	0.64	9.62×10^{-5}
0.08	0.64	8.59×10^{-5}
0.11	0.66	1.11×10^{-4}
0.13	0.66	8.86×10^{-5}

Mg and the lattice. In the β-phase, the ionic conductivity increased monotonically with increasing Mg concentration in the region where $x < 0.09$. In the α-phase, however, the ionic conductivity did not tend to increase at Mg concentrations of $x \geq 0.05$. In the β-phase, the ionic conductivity also tended to remain almost constant at a Mg concentration $x \geq 0.09$. It is thought that the increase in ionic conductivity in the small x region is due to the increase in Mg ion concentration, but the conductivity of Mg ions does not

Table 4 Compositional dependence of migration energies and ionic conductivities of Mg ions for random structures of β-phases at 873 K

| x in β-phase	Migration energy, eV	Conductivity at 873 K, S cm^{-1}
0.02	0.73	9.84×10^{-6}
0.05	0.72	1.83×10^{-5}
0.06	0.72	3.80×10^{-5}
0.09	0.72	5.04×10^{-5}
0.13	0.72	5.27×10^{-5}

change when doped above a certain level, indicating that simply increasing the Mg concentration does not improve the ionic conductivity.

To better understand the Mg ion conductivity behavior, the MD calculated population density of Mg at 1400 K in α-phase ($x = 0.05$) with a random Hf/Nb configuration is shown in Fig. 10. The hopping of the Mg ion directly from 6a site to 6a site is clearly visible. We also confirmed that Mg is trapped in the octahedral Hf vacancy sites and does not contribute to diffusion, and that Mg ions on the diffusion path are trapped to octahedral Mg due to lower valence than Hf and Nb. In both α- and β-phases, two Mg^{2+} ions can be doped per Hf^{4+} vacancy by considering charge neutrality. We confirmed that one of doped two Mg ions tends to occupy the Hf vacancy, but the Mg concentration itself, which contributes to diffusion, increases monotonically (Fig. 9). The Mg ions on the diffusion path are strongly trapped by the Mg located at the Hf vacancy site, which may reduce the concentration of diffusive Mg ions.

Thus, the constant conductivity behavior above a certain Mg ion concentration may be a trapping effect forming a strong binding between Mg at the diffusion path and Mg occupying the Hf vacancy sites.

Based on this significant effect of the Hf/Nb arrangement, we conclude that a uniform valence distribution that does not generate Mg ion traps is desirable for the development of higher Mg ionic conductivity in the α-phase. By increasing the complexity of the cation composition, i.e., high entropy strategy, it might be possible to develop highly ionic conducting phases with averaged potentials and suppressed trapping effects, as recently reported [42].

Fig. 10 Population density for Mg ions in the α-phase ($x = 0.05$) during MD simulation at 1400 K (yellow isosurface). Beige, green, and lavender polyhedra correspond to HfO$_6$, NbO$_6$, and PO$_4$, respectively. The orange sphere indicates Mg ions located at octahedral vacancy sites
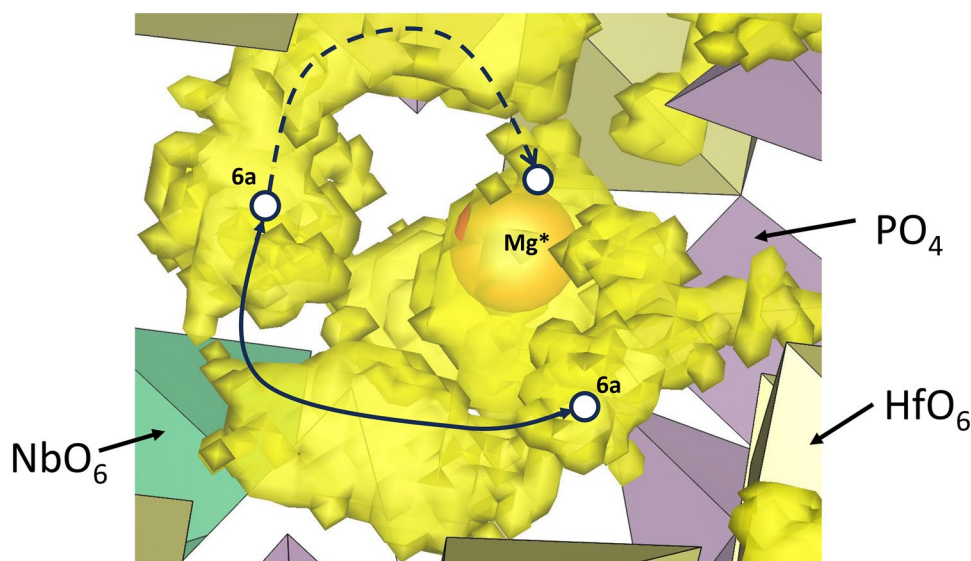
Conclusion

NNP-MD was performed to investigate the phase stability and ionic conductivity of Mg in NASICON-type and β-iron sulfate-type $Mg_{2x}Hf_{1-x}Nb(PO_4)_3$. The results showed that the NASICON-type structure is slightly more stable and also has a higher Mg ionic conductivity than the β-iron sulfate-type derivative. This is consistent with the previously reported experimental results. We found that the Hf/Nb arrangement in the NASICON-type structure strongly affects the ionic conductivity, with the GA derived ordered and stable Hf/Nb arrangement decreasing the ionic conductivity of Mg compared to the random Hf/Nb arrangement. Furthermore, the ionic conductivity increases monotonically with increasing concentration of Mg at low concentrations, but tends to converge to a certain value once a certain concentration is exceeded. This might be due to the trapping effects caused by Mg ions at octahedral Hf vacancies. Therefore, to achieve high ion-conducting phases in $Mg_{2x}Hf_{1-x}Nb(PO_4)_3$ materials, it is considered necessary to maintain a random arrangement of Hf/Nb by processes such as high-temperature sintering and quenching and to adjust the appropriate amount of Mg/Hf to suppress Mg ion trapping.

Declarations

References

1. Van Noorden R (2014) The rechargeable revolution: a better battery. Nature 507:26–28. https://doi.org/10.1038/507026a
2. Kubota K, Dahbi M, Hosaka T et al (2018) Towards K-ion and Na-ion batteries as "beyond Li-ion." Chem Rec 18:459–479. https://doi.org/10.1002/tcr.201700057
3. Tian Y, Zeng G, Rutt A et al (2021) Promises and challenges of next-generation "beyond Li-ion" batteries for electric vehicles and grid decarbonization. Chem Rev 121:1623–1669. https://doi.org/10.1021/acs.chemrev.0c00767
4. Shao Y, Nav Nidhi Rajput JH (2015) Nanocomposite polymer electrolyte for rechargeable magnesium batteries. Nano Energy 12:750–759
5. Zhao-Karger Z, Zhao X, Wang D et al (2015) Performance improvement of magnesium sulfur batteries with modified non-nucleophilic electrolytes. Adv Energy Mater 5:1–9. https://doi.org/10.1002/aenm.201401155
6. Aurbach D, Lu Z, Schechter A et al (2000) Prototype systems for rechargeable magnesium batteries. Nature 407:724–727. https://doi.org/10.1038/35037553
7. Tian H, Gao T, Li X et al (2017) High power rechargeable magnesium/iodine battery chemistry. Nat Commun 8:1–8. https://doi.org/10.1038/ncomms14083
8. Jaschin PW, Gao Y, Li Y, Bo SH (2020) A materials perspective on magnesium-ion-based solid-state electrolytes. J Mater Chem A 8:2875–2897. https://doi.org/10.1039/c9ta11729f
9. Roedern E, Kühnel RS, Remhof A, Battaglia C (2017) Magnesium ethylenediamine borohydride as solid-state electrolyte for magnesiumbatteries. Sci Rep 7:2–7. https://doi.org/10.1038/srep46189
10. Banerjee A, Wang X, Fang C et al (2020) Interfaces and interphases in all-solid-state batteries with inorganic solid electrolytes. Chem Rev 120:6878–6933. https://doi.org/10.1021/acs.chemrev.0c00101
11. Yan Y, Grinderslev JB, Jørgensen M, et al (2020) Ammine magnesium borohydride nanocomposites for all-solid-state magnesium batteries. ACS Appl Energy Mater 3:9264–9270. https://doi.org/10.1021/acsaem.0c01599
12. Li M, Lu J, Chen Z, Amine K (2018) 30 years of Lithium-ion batteries. Adv Mater 30:1800561. https://doi.org/10.1002/adma.201800561
13. Ma S, Jiang M, Tao P et al (2018) Temperature effect and thermal impact in lithium-ion batteries: a review. Prog Nat Sci Mater Int 28:653–666. https://doi.org/10.1016/j.pnsc.2018.11.002
14. Lisbona D, Snee T (2011) A review of hazards associated with primary lithium and lithium-ion batteries. Process Saf Environ Prot 89:434–442. https://doi.org/10.1016/j.psep.2011.06.022
15. Yabuuchi N, Kubota K, Dahbi M, Komaba S (2014) Research development on sodium-ion Batteries. Chem Rev 114:11636–11682. https://doi.org/10.1021/cr500192f
16. Hwang JY, Myung ST, Sun YK (2017) Sodium-ion batteries: present and future. Chem Soc Rev 46:3529–3614. https://doi.org/10.1039/c6cs00776g
17. Tamura S, Araki K, Imanaka N (2016) Trivalent gallium ion conduction in NASICON-type solid. J Asian Ceram Soc 4:390–393. https://doi.org/10.1016/j.jascer.2016.08.002
18. Imanaka N, Tamura S (2011) Development of multivalent ion conducting solid electrolytes. Bull Chem Soc Jpn 84:353–362. https://doi.org/10.1246/bcsj.20100178
19. Nunotani N, Tamura S, Imanaka N (2012) Highly tetravalent hafnium ion conducting solids with a NASICON-type structure. Electrochemistry 80:743–745. https://doi.org/10.5796/electrochemistry.80.743

20. Barth S, Olazcuaga R, Gravereau P et al (1993) Mg0.5Ti2(PO4)3 — a new member of the NASICON family with low thermal expansion. Mater Lett 16:96–101. https://doi.org/10.1016/0167-577X(93)90031-R

21. Aatiq A, Marchoud A, Bellefqih H, Tigha MR (2017) Structural and Raman spectroscopic studies of the two M0.50SbFe(PO4)3 (M = Mg, Ni) NASICON phases. Powder Diffr 32:S40–S51. https://doi.org/10.1017/S0885715617000331

22. Imanaka N, Okazaki Y, Adachi G (2000) Divalent magnesium ionic conduction in Mg 1–2x(Zr 1-xNb x) 4P 6O 24 (x = 0–0.4) solid solutions. Electrochem Solid-State Lett 3:327–329. https://doi.org/10.1149/1.1391138

23. Nakano K, Noda Y, Tanibata N et al (2019) Computational investigation of the Mg-ion conductivity and phase stability of MgZr4(PO4)6. RSC Adv 9:12590–12595. https://doi.org/10.1039/c9ra00513g

24. Tamura S, Yamane M, Hoshino Y, Imanaka N (2016) Highly conducting divalent Mg2+ cation solid electrolytes with well-ordered three-dimensional network structure. J Solid State Chem 235:7–11. https://doi.org/10.1016/j.jssc.2015.12.008

25. Nomura K, Ikeda S, Ito K, Einaga H (1992) Framework structure, phase transition, and transport properties in MIIZr4(PO4)6 compounds (MII = Mg, Ca, Sr, Ba, Mn Co, Ni, Zn, Cd, and Pb). Bull Chem Soc Jpn 65:3221–3227. https://doi.org/10.1246/bcsj.65.3221

26. Ikeda S, Takahashi M, Ishikawa J, Ito K (1987) Solid electrolytes with multivalent cation conduction. 1. Conducting species in MgZrPO4 system. Solid State Ionics 23:125–129. https://doi.org/10.1016/0167-2738(87)90091-9

27. Liang B, Keshishian V, Liu S et al (2018) Processing liquid-feed flame spray pyrolysis synthesized Mg0.5Ce0.2Zr1.8(PO4)3 nanopowders to free standing thin films and pellets as potential electrolytes in all-solid-state Mg batteries. Electrochim Acta 272:144–153. https://doi.org/10.1016/j.electacta.2018.04.015

28. Bekaert L, Akatsuka S, Tanibata N et al (2023) Assessing the reactivity of the Na3PS4 solid-state electrolyte with the sodium metal negative electrode using total trajectory analysis with neural-network potential molecular dynamics. J Phys Chem C 127:8503–8514. https://doi.org/10.1021/acs.jpcc.3c02379

29. Chen C, Ong SP (2022) A universal graph deep learning interatomic potential for the periodic table. Nat Comput Sci 2:718–728. https://doi.org/10.1038/s43588-022-00349-3

30. Larsen AH, Mortensen JJ, Blomqvist J et al (2017) The atomic simulation environment—a Python library for working with atoms. J Phys Condens Matter 29:273002. https://doi.org/10.1088/1361-648X/aa680e

31. Hafner J (2008) Ab-initio simulations of materials using VASP: density-functional theory and beyond. J Comput Chem 29:2044–2078. https://doi.org/10.1002/jcc.21057

32. Kresse G, Hafner J (1994) Ab initio molecular-dynamics simulation of the liquid-metalamorphous- semiconductor transition in germanium. Phys Rev B 49:14251–14269. https://doi.org/10.1103/PhysRevB.49.14251

33. Kresse G, Hafner J (1993) Ab initio molecular dynamics for liquid metals. Phys Rev B 47:558–561. https://doi.org/10.1103/PhysRevB.47.558

34. Kresse G, Furthmüller J (1996) Efficiency of ab-initio total energy calculations for metals and semiconductors using a plane-wave basis set. Comput Mater Sci 6:15–50. https://doi.org/10.1016/0927-0256(96)00008-0

35. Perdew JP, Burke K, Ernzerhof M (1996) Generalized gradient approximation made simple. Phys Rev Lett 77:3865–3868. https://doi.org/10.1103/PhysRevLett.77.3865

36. Perdew JP, Ruzsinszky A, Csonka GI et al (2008) Restoring the density-gradient expansion for exchange in solids and surfaces. Phys Rev Lett 100:136406. https://doi.org/10.1103/PhysRevLett.100.136406

37. Allouche A (2012) Software news and updates gabedit — a graphical user interface for computational chemistry softwares. J Comput Chem 32:174–182. https://doi.org/10.1002/jcc.21600

38. Nakayama M, Nishii K, Watanabe K et al (2021) First-principles study of the morphology and surface structure of LaCoO3 and La0.5Sr0.5Fe0.5Co0.5O3 perovskites as air electrodes for solid oxide fuel cells. Sci Technol Adv Mater Methods 1:24–33. https://doi.org/10.1080/27660400.2021.1909871

39. Miyakawa S, Matsuda S, Tanibata N et al (2022) Computational studies on defect chemistry and Li-ion conductivity of spinel-type LiAl5O8 as coating material for Li-metal electrode. Sci Rep 12:1–11. https://doi.org/10.1038/s41598-022-20289-2

40. Kawai K, Shi X-M, Takenaka N et al (2022) Kinetic square scheme in oxygen-redox battery electrodes. Energy Environ Sci 15:2591–2600. https://doi.org/10.1039/D1EE03503G

41. Yokoyama Y, Nakayama M (2023) Python code for genetic algorithm GmAte.py. https://github.com/NakayamaLab-NITech/GA-for-material. Accessed 16 Jan 2023

42. Zeng Y, Ouyang B, Liu J et al (2022) High-entropy mechanism to boost ionic conductivity. Science 378:1320–1324. https://doi.org/10.1126/science.abq1346